Summer 2019

Surface modified gold nanorods based mercury sensor

Tianqi Luan
Western Washington University, luant2@wwu.edu

Surface modified gold nanorods based mercury sensor

By

Tianqi Luan

Accepted in Partial Completion
of the Requirements for the Degree
Master of Science

ADVISORY COMMITTEE

Dr. Ying Bao, Chair

Dr. Mark Bussell

Dr. Amanda Murphy

GRADUATE SCHOOL

Dr. David Patrick, Dean

Master's Thesis

In presenting this thesis in partial fulfillment of the requirements for a master's degree at Western Washington University, I grant to Western Washington University the non-exclusive royalty-free right to archive, reproduce, distribute, and display the thesis in any and all forms, including electronic format, via any digital library mechanisms maintained by WWU.

I represent and warrant this is my original work, and does not infringe or violate any rights of others. I warrant that I have obtained written permissions from the owner of any third party copyrighted material included in these files.

I acknowledge that I retain ownership rights to the copyright of this work, including but not limited to the right to use all or part of this work in future works, such as articles or books.

Library users are granted permission for individual, research and non-commercial reproduction of this work for educational purposes only. Any further digital posting of this document requires specific permission from the author.

Any copying or publication of this thesis for commercial purposes, or for financial gain, is not allowed without my written permission.

Your Name: Tianqi Luan

Date: July 8th, 2019

Surface modified gold nanorods based mercury sensor

A Thesis
Presented to
The Faculty of
Western Washington University

In Partial Fulfillment
Of the Requirements for the Degree
Master of Science

by
Tianqi Luan
July 2019

Abstract

The high toxicity of mercury in the form of inorganic vapor and organic compounds has become a major concern leading scientists to investigate more accurate and effective methods for the quantification of residue mercury in drinking water, aquaculture products and industrial wastes.

In this research, we designed a mercury sensor based on the amalgamation between mercury and gold nanorods (AuNRs) which relate the longitudinal surface plasmon resonance (LSPR) peak shift induced by aspect ratio (AR) change after amalgamation. However, most of AuNRs synthesized based on seed mediated methods use either citrate or hexadecyl trimethyl ammonium bromide (CTAB) as surface stabilizing agent suffers from stability problems in high ion concentration and severe pH.

Surface modifications were introduced to make this system more stable, sensitive and capable of real-world application. Layer-by-layer (LbL) method with polyelectrolytes is commonly used for adjusting both surface charge and thickness of polymer shell. AuNRs covered with different numbers of polyelectrolyte layers were characterized with Zeta-potentiometer and UV-Vis spectrometer then same mercury sensing process was carried out. Ligand-exchange was introduced as another surface modify method. Poly(ethylene glycol) methyl ether thiol (PEG-thiol) was chosen for its strong affinity to gold surface and ability to replace CTAB as stabilizing agent. Ligand exchanging brought not only better stability but also selectivity and sensitivity to mercury sensing. To explain the improvement in sensitivity, the thiol-Hg-thiol complex model was proposed and evaluated.

Acknowledgements

I thank all my committee members for their great instructions. Thank all members from Bao's group for our valuable discussions especially John Crockett for working on this project with me, Gary Carlton and stock room for their support, Dr. Mike Kraft from AMSEC for his assistance on various instruments. Alexi Guddal, Stacey Maxwell, Steve Sible, Dr. Elizabeth Raymond and Dr. Spencer Anthony-Cahill's great work and support. Dr. John Antos, Dr. James Vyvyan for their guidance as graduate student advisor. Dr. Spencer Berger and Amy Cully as instructor for teaching responsibilities. Thank Western Washington University and chemistry department for providing me this great opportunity.

Great thanks to Dr. Ying Bao, Dr. Mark Bussell and Dr. Amanda Murphy for being my committee, guiding me through the whole research process and their input in reviewing this thesis.

Contents

List of Tables and Figures

Chapter 1 - Introduction

1.1 Nanomaterials

1.1.1 Background

Nanoscale material, despite being a relatively new concept, exist widely in nature. Volcanic ash, smoke, sea spray all contain nanoscale particles. The usage of nanoparticles can also be traced back to ancient Rome in the famous Lycurgus cups. Yet it was not until 1857, Michael Faraday in his research paper provided the first scientific definition: “It is well known that when thin leaves of gold or silver are mounted upon glass and heated to a temperature that is well below a red heat (~500 °C), a remarkable change of properties takes place, whereby the continuity of the metallic film is destroyed. The result is that white light is now freely transmitted, reflection is correspondingly diminished, while the electrical resistivity is enormously increased."[1]

Fig. 1 Michael Faraday’s colloidal gold, one of the earliest examples of metallic gold colloids, made by Michael Faraday over 150 years ago (Michael Faraday's gold colloids https://www.rigb.org/our-history/iconic-objects/iconic-objects-list/faraday-gold-colloids (accessed Jul 16, 2019).)

Despite the fact that nanoparticles have been around for a long time, the two major innovations marking the current nanoscience revolution happened in the 1980s. In the year 1982 the scanning tunneling microscope was invented, and several years later in 1984 that C_{60}, named Buckminsterfullerene for the famed architect, futurist and philosopher, was produced.

The unique properties that make nanoscale materials fascinating can be concluded to three aspects: quantum effects, biological reactions and interface. When sizes of solid matters are in the visible scale compared to what can be seen in optical microscopes, there is little difference in the properties of the particles. But when particles are created with dimensions of about 1–100 nanometers (where the particles can be “seen” only with electron microscopes), the materials’ properties change significantly from those

at larger scales. This is the size scale where so-called quantum effects rule the behavior and properties of particles. Once materials get in this scale, their properties become size-dependent. Hence, we are able to modify their melting point, fluorescence, electrical conductivity, magnetic permeability, and chemical reactivity for a specific purpose.

Second of all, most of biology occurs at nanoscale. For example, hemoglobin, the protein that carries oxygen through the body, is 5.5 nm in diameter. A strand of DNA, one of the building blocks of human life, is only about 2 nm in diameter. One good example for nanomaterial applications in biology is the bio-barcode assay. The basic process, which attaches "recognition" particles and DNA "amplifiers" to gold nanoparticles, was originally demonstrated at Northwestern University for a prostate cancer biomarker following prostatectomy.[2] This process is intended to amplify the fluorescence signal when hairpin-DNAs are attached to disease-specific biomarkers in the blood.

The third reason is related to surface and interface. For any bulk material, interfaces tend to have drastically different properties. Nanoscale particles inherently have larger surface area than material with similar mass or volume. One benefit of greater surface area is improved reactivity: nanostructured materials can be used to create better catalysts. As a result, catalysis by engineered nanostructured materials already accounts for about one-third of the U.S.—and global—catalyst markets, affecting billions of dollars of revenue in the oil and chemical industries.[3] An everyday example of catalysis is the catalytic converter in a car, which reduces the toxicity of the engine's fumes by catalyzing the reaction between CO, unburned hydrocarbon and oxygen and then convert them into inert gas like CO_2 and water vapor. Nano-engineered batteries, fuel cells, and catalysts can potentially use enhanced reactivity at the nanoscale to produce cleaner, safer, and more affordable methods of producing and storing energy.

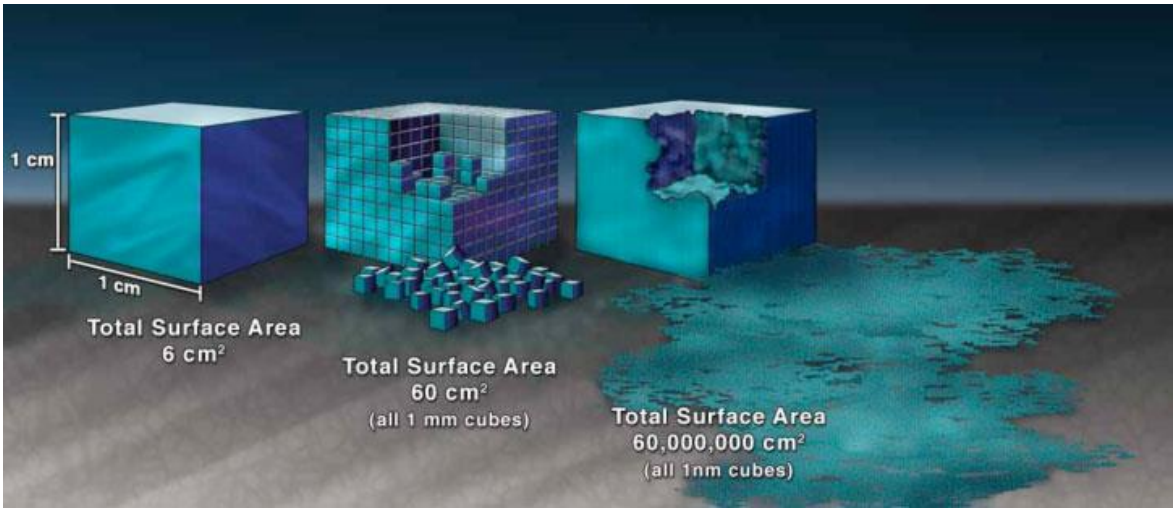

Fig. 2 A comparison of surface area between materials with the same total mass (What's So Special about the Nanoscale? https://www.nano.gov/nanotech-101/special (accessed Jul 12, 2019).)

1.1.2 Synthesis methods

Nanomaterials can be synthesized with different methods like gas condensation, chemical precipitation, ion implantation, pyrolysis and hydrothermal synthesis, etc. All of those methods can be roughly classified into two groups: top-down and bottom-up.

In top-down methods like attrition, nanoparticles are generated from bulk materials broken into small pieces. A typical attrition synthesized nanoparticle is silicon. In the manufacture process, coarse raw material is dumped into a ball mill filled with grinding media. Then by rotating the chamber, coarse silicon will be ground into powder. Bottom-up synthesized nanomaterial are built from a number of atoms or ions generated from a source then condensed into a nano-scale particle. Inert-gas condensation is one of the bottom-up synthesis examples. In inert-gas condensation, metal atoms on an anode are evaporated into inert gas at high temperature. The plasma is then cooled until it becomes oversaturated at which point the atoms will begin to nucleate homogeneously from the vapor stream. Clusters of particles form and sinter, either with another stream of gas (the quench gas), or a chilled surface. As-synthesized particles are collected and proceed into post-processing steps. Inert-gas condensation is usually used to generate carbon blacks, silicon dioxide and titanium dioxide.[4]

Another bottom-up synthesis method: vapor phase deposition, usually known as chemical vapor deposition (CVD) or physical vapor deposition (PVD).[5] Difference is, the material in CVD came from precursor gas and substance in a reaction furnace, while PVD generates all material by physically evaporate liquid or solid source material. CVD is used in the production of various types of materials including graphene, carbon nanotubes and even diamonds.

Fig. 3 A gem cut from synthetic diamond made by Apollo Diamond from CVD (Brilliant Earth https://www.brilliantearth.com/ (accessed Jul 12, 2019).)

All of the methods introduced above require expensive and complicated or bulky instructments. That is why in research labs, wet chemistry methods are more popular in terms of nanoparticle synthesis. Most of the wet chemistry methods are based on either colloidal or sol-gel synthesis. Sol-gel method is widely used in metal oxide material fabrication which includes a colloidal suspension (sol) acting as a precursor for an integrated network (gel). Sol-gel system synthesized nanoparticles can be found mainly in organic-inorganic hybrids, photonic crystals, ferroelectric coatings, and photocatalysts.[6] Michael Faraday synthesized colloid gold by accidentally washing gold leaf with acid and poured some reducing waste into the same bottle.[1] After a one and a half centuries, researchers are still using similar methods to create nanoscale materials. Metallic nanoparticles can be created by reducing metallic salt in certain condition and with the presence of surface capping agent. The capping agent will also act as colloids in solution. The reduction reaction will form a supersaturated metal ion solution inside the colloids which nucleates to form nanoparticles.

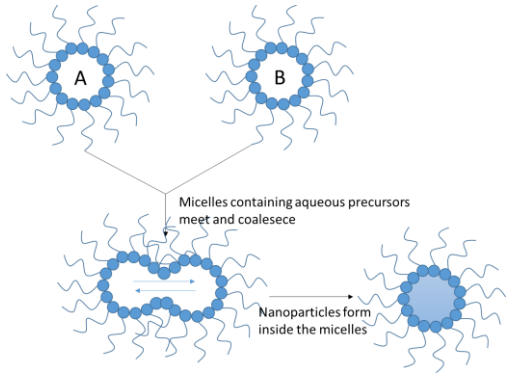

Fig. 4 Schematic for sol-gel nanoparticle synthesis process

In a very common and classic colloidal synthesis for the gold nanoparticles, $AuCl_4^-$ solution is added to pre-dissolved high concentration n CTAB (act as capping agent and forms colloids) the reduced by either sodium citrate or $NaBH_4$.[7]

1.1.3 Characterization

As we mentioned above, many instruments were made for the purpose of nanoscale characterization and the invention of these instruments also contributed to the development of nanotechnology.

Scanning Electron Microscope (SEM) and Transmission Electron Microscope (TEM) are used for imaging and sizing nanoparticles with an electron beam. One example for TEM's characterization ability, especially for metal nanoparticles and semiconductors, is to determine the lattice orientation. High Resolution TEM (HR-TEM) has the resolution that can reach atomic level. Since most of nanoparticles surface properties are facet-based, especially catalysis reactions, it is very important for us to identify all the facets of the nanoparticle of interest. Before HR-TEM was invented, electron-diffraction was used to do lattice structure analysis but it is not surface-specific and can't be directly viewed. With HR-TEM, the lattice pattern can be directly imaged and analyzed. Nanoparticle surface properties are important and more than just facet orientation; surface charge, roughness and contents have drastic effects on the overall surface properties. Surface charge, characterized by Zeta-potentiometer, is vital for any nanoparticles that are dispersed in solution. In order for the nanoparticles to remain dispersed without aggregation, all of the nanoparticles in solution should carry at least a certain amount of surface charge so the electrostatics forces will repel them from each other. Energy Dispersive X-Ray Spectroscopy (EDS)

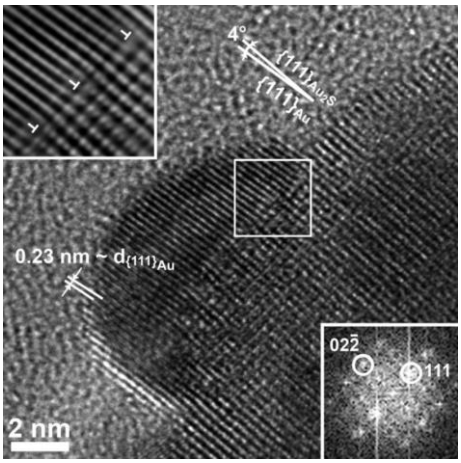

Fig. 5 HR-TEM image of different lattice pattern on a piece of silicon wafer (Reprinted (adapted) with permission from Langmuir 2008 24，8, 4289-4294. Copyright (2008) American Chemical Society)

and X-Ray Photon Spectroscopy (XPS) are used for surface composition analysis. Crystal structures in the bulk part of nanoparticles are determined by either X-Ray Powder Diffraction (XRD) or Low-Energy Electron Diffraction (LEED).[8]

One of nanoparticles special thermal and optical properties come from its high surface area to volume ratio. Especially for metallic nanoparticles, Surface Plasmon Resonance (SPR) happens on their surface which makes them very ideal for light harvesting and protein labeling etc.[9] Since SPR is the resonance of electromagnetic wave at a certain wavelength, absorption spectroscopies are usually used to find out the specific resonating wavelength. At the resonating wavelength, the absorption of analyte should increase significantly. Ultraviolet-Visible Spectroscopy (UV-Vis-NIR or UV-Vis) is an easy and straightforward way to measure sample's absorption curve between UV and near-IR region (depends on specific model) which is widely used in SPR peak characterization.

1.1.4 Properties and applications

The reason nanotechnology has seen a huge leap in the last few decades is because research has shown huge potential for nanomaterials in real-world application. Their fascinating electronic and optical properties are consequences of their dimensions. The dimensions of these particles make them ideal candidates for the nanoengineering of surfaces and the fabrication of functional nanostructures.

One of the most representative example of nanomaterial application is the use of carbon nanotubes (CNTs). CNTs are tube-shaped nanoparticles built from a single layer of carbon atoms giving them very special electrical properties. Elemental carbon is usually considered a type of insulator as it has a large band gap at room temperature. But carbon nanotube's bandgap is so small that it can be considered as moderate semiconductor.[10] This property of CNT's has created a whole field of potential applications such as acting as a probe tip in scanning probe microscopes or in display devices.[11] Because of the nearly one-dimensional electronic structure, electronic transport occurs ballistically without any scattering. In other

words, CNTs can carry high currents long distances without heating.[12] Superconductivity has also been observed, but only at low temperatures, with transition temperatures of 0.55 K for 1.4-nm-diameter single wall-CNTs.[13]

Metallic nanoparticles have also found potential uses in catalysis[14], light harvesting[15] and medical therapy[16], etc. Many photonic and photothermal properties of metallic nanoparticles came from the strong plasmonic electromagnetic field resulting from localized surface plasmon resonance (LSPR). This effect brings enhancement of rates for linear optical processes like absorption, fluorescence, and Rayleigh or Raman processes as well as nonlinear processes like second harmonic generation (SESHG)[17] and surface enhancement fluorescence.[18] Raman signals can be enhanced by up to 10^6 folds by the process of surface enhancement Raman spectroscopy (SERS). If the analyte molecule is located at the "hot-spot" in between the assembled plasmonic nanoparticles, the enhancement factor can reach 10^{14}.[19]

One of the most popular applications of this kind of signal amplification is in colorimetric assays. In many biosensing processes, the robust strategies of enzyme-labeling on the antibody or DNA can dramatically improve the possibility for sensitive detection of DNA, RNA, protein, and small molecules.[21] The result is analyzed with the color change of the oxidation of enzyme-specific chromogenic substrates (3,3',5,5'-tetramethylbenzidine (TMB) and 2,2'-azino-bis(3-ethylbenzothiazoline-6-sulfonic acid) (ABTS)) from colorless into colored products, and the intensity signal of the solution can be analyzed by a microplate reader or the naked eye.[22] But the sensitivity is limited by the monochromatic color change. Introducing metallic nanoparticles whose absorption band will change according to different concentrations of analyte can improve the accuracy of detection.

1.2 Gold nanoparticles

Since the late 1990s, nanoparticle and nanotechnology has drawn more and more attention, nanotechnology and material has become a vital part of innovation. Among all types of nanomaterials,

noble-metal nanomaterials with their unique size-dependent properties have attracted the most attention. Especially gold nanoparticles, which were one of the first nanoscale nanomaterials synthesized in human history. Colloidal gold particles were used to stain glasses since the 4th century in ancient Rome.[23] In the year 1676, Johann Kunckel first proposed that the pink color in Lycurgus Cups came from small metallic gold particles that are not visible to the human eye.[24] Most of the early studies on gold nanoparticles were based on spherical and quasi-spherical nanoparticles because they are the most thermodynamically favorable structure and hence easier to synthesize. The first standardized wet chemistry synthesis process for gold spherical nanoparticles were proposed in 1951 by James Hillier and his colleagues[25] by mixing sodium citrate as a reducing agent in gold chloride solution. Most gold nanoparticle synthesis followed this method until morphology growth mechanism is studied more thoroughly in early 2000s. In the mid-1990s, gold nanorod synthesis was achieved by electrochemically reducing gold ions in a rod-shaped template.[26] This method got popular for being the first successful trial in anisotropic nanoparticle synthesis yet suffers from low yield. In most recent works, morphology with higher order complicity are achieved by tuning reaction conditions. By using surfactant to restrict the growth process or introducing template into the procedure, more complex structures can be achieved.[27]

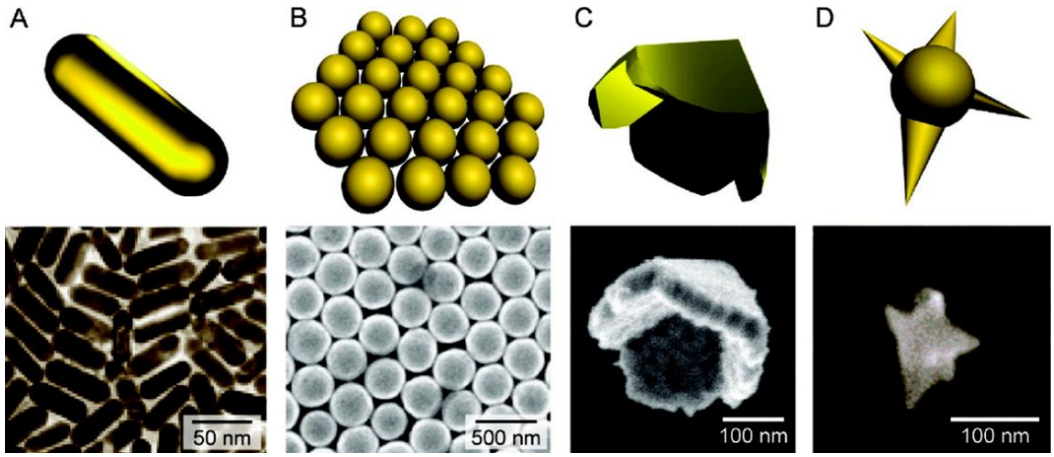

Fig.6 Synthesized and fabricated anisotropic gold nanoparticles. (A) Nanorods.(1) (B) Arrays of nanoshells (interiors are silica).(3) (C) Nanopyramids. (Scanning electron micrograph courtesy of

Jeunghoon Lee, Northwestern University.) (D) Nanostars. (Reprinted (adapted) with the permission from ACS Nano2008 24, 612-616. Copyright (2008) American Chemical Society)

Among all the morphologies in noble metal nanoparticles, gold nanorods are the first successful example of an anisotropic plasmonic nanostructure synthesized by wet chemistry.[28] With its unique tunable optic (plasmonic) property, gold nanorods have become the ideal candidate for applications like solar harvesting in photovoltaics,[29] surface enhanced spectroscopies,[30] and sensing,[31] etc.

1.2.1 Gold nanorods: synthesis process

The growth mechanism of anisotropic nanostructures has been fascinated for researchers. Because the growth of nanoparticles is determined by the kinetic balance between nucleation rate to facet-specific growth.[32] A higher nucleation rate leads to higher spherical byproduct yield because of non-facet specific growth. Specifically for noble metal nanoparticles, pentagonal pyramidal shaped seeds are desired because most of the facet-specific growth of a rod-shaped nanoparticle happens in the five (111) twin boundaries along the direction of elongation.[33] As Fig. 7 shown, the Au^{+} reduced by citrate takes place in the areas of highest surface energy in decahedra (the wedges between the decahedra surfaces). While Au^{+} keeps depositing onto the wedges, (111) facets are continuously being reconstructed and (100) facets are being elongated. These kinds of areas in decahedra are caused by intrinsic geometric misfit and resolved by HR-TEM image (Fig. 7).

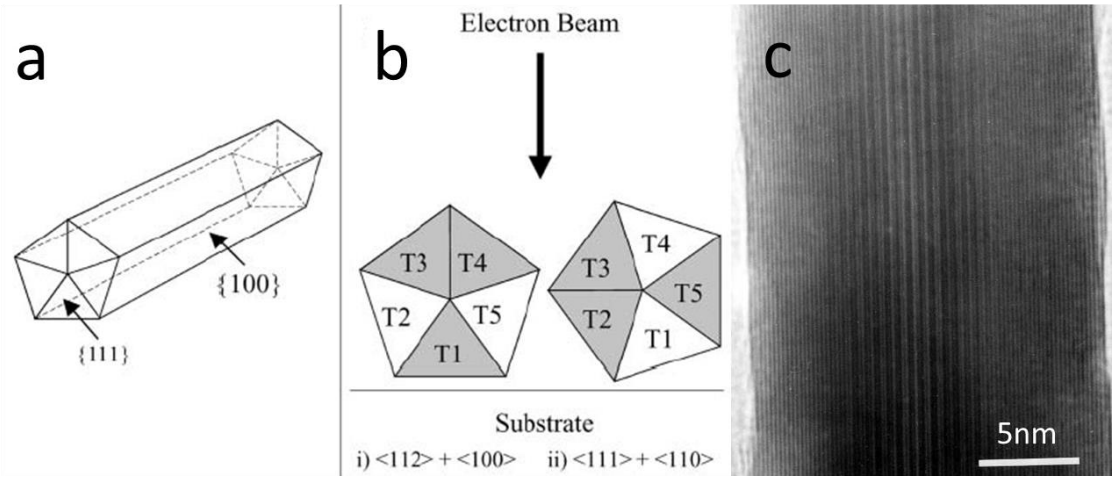

Fig. 7 Proposed elongation of a decahedral seed to gold nanorod. (a) Idealized 3-D morphology showing {111} end faces and {100} side faces. (b) Crosssection of nanorod structure showing arrangement of twins T1 to T5, and possible orientations of domains with respect to the electron beam. (c) HRTEM image of gold nanorod viewed down the <112>/<100> zone. The fringes are modulated in the central region of the twinned crystal into wider stripes due to double diffraction arising from the superposition of twin domains aligned along different zones (see (b)). (Reprinted (adapted) with the permission from J. Mater. Chem., 2002, 12, 1765–1770. copyright (2002) Royal Society of Chemistry (Great Britain))

Another aspect contributing to rod growth in AuNRs is the ligand used to stabilize the AuNRs in solution. In most of the wet chemistry AuNR synthesize recipe known to us, Cetyltrimethylammonium Bromide (CTAB) is used as the stabilizing ligand. Research has proved that CTAB bilayers, Br^- specifically, select against (111) facets by a process of oxidative etching.[34] In other words, CTAB bilayers will strongly bond to (100) facets and form CTA-Au-Br complex which slow down the growth in this direction.[35] There are researches indicate that using binary surfactant mixture, nanorods with extreme monodisperse dimension can be synthesized.[65] The CTAB surfactant method was picked in this project for the low-cost and easy preparation.

1.2.2 Optical property: Gold Nanoparticles

Pioneering studies on surface plasmonic properties of noble metal like Ag and Au has started since over a century ago. Gustav Mie recognized the interaction between free electrons and light can give a rise to collective oscillations.[36] When metal particles are exposed to light, the free electrons in the conduction band of metal oscillate collectively with the electromagnetic wave. The electrons oscillating around the surface form a dipole along the direction of the electric field of light. When the frequency reaches a certain point, the amplitude of oscillation will reach a maximum. This effect, known as surface plasmon resonance (SPR), has made Ag and Au nanoparticles very ideal in applications like light harvesting and photothermal therapy[37], etc. When free electrons in a conduction band oscillate in a finite volume (the oscillation can propagate across the surface as a charge density wave) the plasmon localized to each particle (Fig. 8).[38]

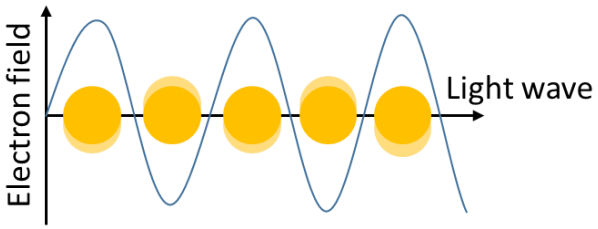

Fig. 8 Localized surface plasmon resonance on metallic nanoparticles

Because the resonance wavelength effect for surface plasmons is directly related to the dimension of nanoparticles this allows us to tune the desired peak absorbance position. Gold nanorods, as a type of anisotropic nanoparticle, possess multiple plasmon resonance modes. The two resonance modes which correspond to the width and length of nanorods are referred as transverse surface plasmon resonance (TSPR) and longitudinal surface plasmon resonance (LSPR) as shown in Fig. 9. And what makes nanorods more fascinating is the resonance wavelength can be easily controlled by tuning the length/width/overall aspect ratio of nanorods. Especially for the LSPR mode, the peak absorption for LSPR mode can be adjusted from visible (~600nm) all the way to near IR (~1200nm) based on the synthesis procedure.

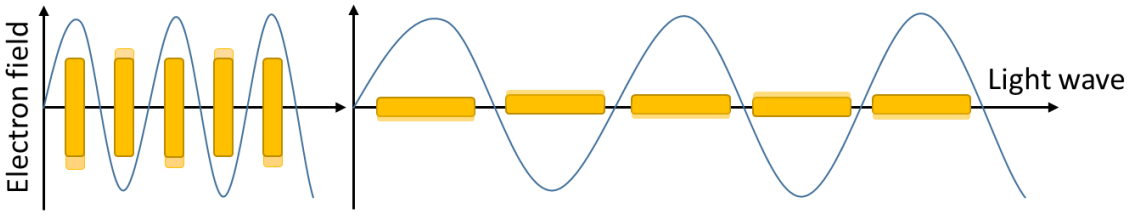

Fig. 9 Two resonance modes on a nanorod, left: TSPR, right: LSPR

1.3 Gold Nanorods for Mercury Sensing

1.3.1 Mercury: toxicity

The toxicity of mercury was first realized by the world in the early 19th century. The infamous Minamata disease was officially identified as a largescale mercury poisoning incident caused by residents in Minamata consuming fish and shellfish products containing high concentrations of mercury.[39]

The toxicity and environmental hazards of mercury mainly come from the fact that mercury is extremely stable in fish and shellfish in the form of methylmercury, a highly toxic mercury organic compound. Also, improperly disposed industrial waste that contains Hg^{2+} is a main source of mercury contaminant in drinking water[40] which is known to cause kidney damage. The strong affinity of gold nanoparticles to inorganic mercury makes them ideal for removing mercury in vapor[41] and drinking water.[42] Detecting Hg^{2+} ions in drinking water mainly relies on Inductively Coupled Plasma-Mass Spectroscopy (ICP-MS) or Cold Vapor Atomic Absorption Spectroscopy (AAS).[43]

1.3.2 Local contaminants

The beautiful city of Bellingham, in which WWU is based, also had a mercury contaminant problem for a long period of time in the previous century. The location where is now the downtown waterfront park was a pulp mill and oil storage facility owned by Georgia Pacific for decades. According to a study done by Washington State Department of Ecology,[44] the mercury content in Bellingham bay water sample is averaging at about 0.1 nmol/g[45] or 0.1 µM which is considered decent for sea water but still about 10 times higher than the state's standard for ground water.[46] As one of the primary contaminants in all kinds of water standards, the test method for mercury detection has also been standardized. Sampling for environmental samples is carried out by simultaneously extracted metals in water and waste by ICP-MS with acid volatile sulfides (AVS).[47]

1.3.3 Major challenges

Instrument based mercury ion sensing has been the standard for years. It has certain problems, for example, both ICP-MS and AAS are expensive instruments which are also not accessible in many parts of the world. Plus, methods like AAS requires excessive sample preparation: cold- vapor AAS is used specifically for mercury detection because mercury is the only metal that has enough vapor pressure at ambient temperature. For water based samples, mercury is oxidized with nitric acid and sulfuric acid to Hg^{2+} then reduced with $SnCl_2$, and the vapor atomization can then be carried out.[48] The Acid Volatile

Sulfides process before ICP-MS measure is even more complicated. It is a method that requires multiple strict conditions: because the sulfide degrades quickly in the presence of oxygen, sediment samples for SEM/AVS analysis must be kept under rigorously anoxic conditions from the moment they are sampled[49] and samples should be kept at 4 ^{o}C to keep the bacterial metabolism from degrading sediments; the recommending storage time of sample before testing is no longer than 14 days.

1.3.4 Advantages with AuNRs based mercury sensor

For the reasons above, researchers have tried to introduce nanoparticle-based mercury sensors. Mercury is a kind of metal that exists as a liquid at room temperature, and can “dissolve” other metals to form an alloy as a result. The phase of the resulting alloy will depend on the ratio of mercury in the alloy. The amalgam process comes from metallic bonds forming between atoms and mercury can form amalgam alloy with almost all kinds of metal. For example, the amalgam alloy containing silver and mercury has been used as a filler in dentistry.

The history of gold amalgam and its application in gold refineries can be traced to the gold rush era. Mercury was deposited inside a copper drum where the gold ore would be extracted (high pressure water stream is usually used to help with the mixing). Then the mercury coating would be scraped off and heated to evaporate the mercury.[50] The amalgam process in ore refining was very popular for it is relatively effective and low-cost. This method is prohibited and has been replaced by more environment friendly methods. Yet it is still used in some smaller scale refineries (illegally) and in a lot of developing countries. In the research carried out by Lynne Katsikas et al., mercury amalgam with colloid silver is examined[51] with UV-Vis spectroscopy. In this work, the absorption of mercury ion on silver nanoparticles model is proposed and the blue-shift on silver nanoparticles UV-Vis absorption peak is explained by formation of mercury shell around silver particles. The mechanism of mercury amalgam on noble metal nanoparticles

also fascinates researchers. The amalgam process is monitored in different ways with a variety of instruments.

Dark-field Scattering Microscopy is one powerful tool for this study because it allows real-time monitoring this amalgam process.[52] The formation of an alloy is demonstrated as a homogeneous attaching of Hg^{2+} followed by amalgamation. This result is verified by Wang et al. who deposited gold nanorods on ITO substrates and control the deposition of Hg^{2+} on nanorods surface by using cyclic voltammetry.[53] The elemental distribution on nanorods surface was characterized with EDX.

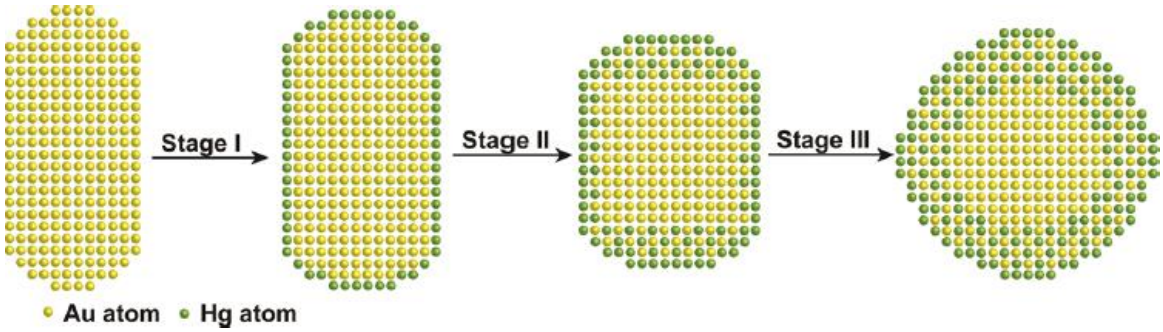

Fig. 10 Amalgam process demonstrated on a gold nanorod (Reprinted (adapted) with permission from *Environmental Science & Technology* 2012, 46 (17), 9557 Copyright (2012) American Chemical Society)

The LSPR peak position closely related to aspect ratio and shape of gold nanorods is confirmed by either experiment or simulation.[54, 55, 56] We already observed that gold nanorods after amalgam tend to deform into spherical shaped gold nanoparticles, the wavelength of the LSPR resonance mode will show substantial blue shift after amalgam. There are multiple works relating the peak shift to mercury amount in order to make a mercury detector.[57, 58]

Since there was a decent amount of work done on gold nanoparticles-based mercury sensors, the mechanism of Hg^{2+} onto gold nanoparticles has been abbreviated into different models. Wang et al. believes Hg atoms attach homogeneously onto surface of AuNRs (Fig. 10). Then mercury atoms etch into AuNRs to form Au-Hg alloy. Hg, as a liquid phase metal at room temperature, after forming the alloy will naturally decrease the aspect ratio.

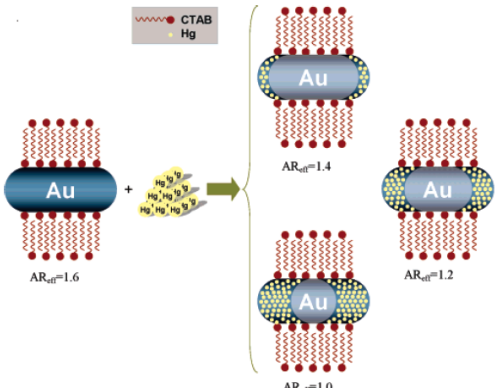

Fig. 11 Schematic diagram showing amalgamation of Hg into AuNRs (Reprinted (adapted) with permission from *Analytical Chemistry* 2006, 78 (2), 445 Copyright (2006) American Chemical Society)

Rex et al. proposed an etching model in their work (Fig. 11). This is mainly based on the active site of AuNRs located on both tips of nanorods.[59] Also based on the fact CTAB bilayers have a higher affinity on {1,0,0} facets on AuNRs. The shielding effect restricts amalgamation of Hg on lateral side of the nanorods. Most of the work listed above was done based on gold nanorods that are stabilized with CTAB in solution. Yet in our research we found out that the concentration of residual CTAB plays a major side effect on the detection result which will be discussed later in the results section. We also designed a series of experiments quantifying the effect of CTAB residue on Hg^{2+} attaching to AuNRs.

To eliminate the shielding effect caused by the CTAB bilayer but still retain the AuNRs dispersion in water, we need a new ligand with stronger affinity to gold and be water-soluble. Poly(ethylene glycol) thiol (PEG-thiol) ligand was selected as the best of all candidates, for the following reasons: a. Thiol group on the end can form Au-S bond with AuNRs which make ligand exchange spontaneous and easy; b. Poly(ethylene glycol) hydrophilic chain keep AuNRs soluble in water. Thiol group ended polymers are commonly used as surface modification ligand on all kinds of gold nanoparticles for the “sulfur-gold bond” formed between gold surface and sulfur atom in thiol group. The mechanism of this nanoscale interaction is still in debate[60] yet this system has been applied in various fields of current nanoscience research, materials science, inorganic chemistry and surface science.

Chapter 2. Experimental

2.1 Chemicals and Instruments

Cetrimonium bromide (CTAB), chloroauric acid ($HAuCl_4$), methoxypolyethylene glycol thiol (PEG-SH), silver nitrate ($AgNO_3$), L-ascorbic acid (L-AA), sodium borohydride ($NaBH_4$), mercury chloride ($HgCl_2$), chromium chloride ($CrCl_3$), barium sulfate ($BaSO_4$), Poly(styrenesulfonate) (PSS, MW~70,000), Poly(diallyldimethylammonium chloride) (PDADMAC, MW~240,000), hydrochloric acid (HCl) are purchased from Sigma-Aldrich.Jasco V-670 UV-Vis-NIR Spectrometer (UV-Vis), Delsa Nano-HC DLS/ELS (Zeta-potentiometer function used), Jeol 7200 Scanning Electron Microscope with EDS, BSE, and STEM detectors (STEM detector and EDS detector used)

2.2 Procedure

2.2.1 Seed solution synthesizing

Gold nanorods were synthesized by using a seed mediated method.[61] This method was picked for it is easier for scaling up and is less dependent on strict environment control. Seed solution was prepared by first dissolving 364 mg CTAB in 10 mL nanopure water, then dissolving the CTAB by heating the vial in a 35 ^{o}C water bath while sonicating. To the fully-dissolved solution, 250 μL 0.01M $HAuCl_4$ solution was added, and stirred for 1 min at room temperature. Reduction process was done by adding 0.6 mL 0.01 M freshly-prepared $NaBH_4$ aqueous solution following by 2 min shaking then kept at room temperature (25 ^{o}C) for 1 h.

2.2.2 Growth for NR with absorption band at about 800nm

Growth solution was made by dissolving CTAB into 40 mL nanopure water to make a 0.1 M CTAB solution. Then 2 mL 0.01 M $HAuCl_4$ was added to 40 mL 0.1 M CTAB aqueous solution. Solution pH was adjusted by adding 0.8 mL 1 M HCl. Then 0.4 mL 0.01 M $AgNO_3$ was added to assist the growth process. The reducing process was carried out by adding 0.32 mL 0.1 M L-AA and vigorously shaking until the solution becomes

colorless (growth solution container needs to be wrapped in aluminum foil starting from this step). Seeding was done by pipetting 96 μL pre-made seed solution into growth solution. The growth medium was left inside water bath set at 35 °C overnight.

2.2.3 Growth for NR with absorptions band at about 880nm

Same 0.1 M 40 mL CTAB aqueous solution was prepared, followed by dissolving 6 mg hydroquinone at 45 °C. Afterwards 333 uL 0.015 M $HAuCl_4$ was added which made solution turn yellow, then shook till solution become colorless. $AgNO_3$ was dissolved in nanopure water to make 24 mM $AgNO_3$ solution, then 200 μL freshly prepared $AgNO_3$ was added into growth solution. As-prepared seed solution 10 μL was added into growth solution followed by 2min stirring and growth overnight under room temperature.

2.2.4 Growth for NR with absorption band at about 1100nm

CTAB solution with the same 0.1 M molarity was prepared into 10 mL solution. Hydroquinone 6 mg was added then dissolved at 45 °C while sonicated. Same 333 μL 0.018 M $HAuCl_4$ was prepared followed by stirring for two minutes till colorless. Then, 200 μL $AgNO_3$ (24 mM) was added at 25 °C followed by 2 min stirring. HCl (1.0 M) was introduced in solution to adjust pH. In this synthesis, the pH was adjusted by adding 20 μL 1.0 M HCl into growth solution. The solution was stirred for 1 min before seeding then 150 μL pre-made seed solution was added and the solution was left overnight aging in water bath at 45 °C.

2.3 Purification Methods

2.3.1 Purification nanorod

All nanorod solutions were distributed into 1.5 mL centrifuge tubes then centrifuged at 12500 rpm for 8 min at 30 °C. The supernatants was removed from the centrifuge tube then re-dispersed the sediment in 1 mL nanopure water. The same process was repeated for two times.

2.3.2 Separation rod from byproducts (spheres, cubes)

Purified rod solution was re-distributed into 1.5 mL centrifuge tubes and centrifuged at 4000 rpm (2000xg) for 8 min. After centrifuging, rods were should still dispersing in supernatant while most of byproducts were condensed and formed sediments at bottom. Supernatant part was collected for further use.

2.4 Surface Modification

2.4.1 PEG-SH ligand exchange nanorod

PEG-SH 10 mg was weighed and added into 10 mL purified rod solution under vigorous stirring. Keep stirring for an hour. All nanorod solution were distributed into 1.5 mL centrifuge tubes then centrifuged at 12500 rpm for 8 min at 30 ^{o}C. Supernatants was removed from the centrifuge tube and the sediment was re-dispersed in 1 mL ethanol. Repeat the same process for three times.

2.4.2 Layer-by-layer polyelectrolytes loading

PSS was dissolved in nanopure water into 10 mg/mL solution. PDADMAC was also dissolved in nanopure water at 10 mg/mL. Nanorod solutions were purified as stated above, but the sediment after centrifuging was dissolved in 1 mM NaCl solution rather than nanopure water. The as-prepared nanorod solution was transferred into a 20 mL glass vial then add as-prepared PSS 10 mg/mL stock solution. The volume ratio between rod solution and PSS solution was kept at 5/1. Purification was required to remove any extra polymer. Second layer of PDADMAC can be applied with the same method. More polyelectrolyte layers can be applied in a repetitive manner.

2.5 Sensing process

As-synthesized AuNR solution was heated in water bath and sonicated till CTAB/hydroquinone dissolved completely. Then all AuNR solutions were standardized in concentration by measuring UV-Vis spectrum absorption intensity and dilute the solution until the intensity of LSPR peak was at about 0.3. All AuNR solution was purified with the method stated above. Sensing process was carried out by mixing 300 μL

rod solution and 10 μL standardized mercury solution (0, 0.05, 0.1, 0.15, 0.2, 0.25mM) in 1.5 mL centrifuge tubes then incubated at room temperature for 20 min. Reducing agent was prepared by making 1.67 mM NaBH4 stock solution while waiting. Hg(II) was reduced by adding 300 μL NaBH4 solution. A sample with no mercury added was included every sensing batch acting as control.

Chapter 3. Results and Discussion

3.1 Rod synthesis

Gold nanorods were synthesized with seed mediated method. Characterization was carried out after purification on Jasco UV-Vis-NIR Spectrometer and JEOL Field Emission Scanning Electron Microscope.

Aspect ratio of the synthesized nanorods was conducted by measuring each individual nanorod in ImageJ and averaging the data afterwards.

The relationship between the nanorods aspect ratio and LSPR mode wavelength was further proved by our result from UV-Vis and SEM. For the 800 nm rod growth recipe, the nanorods obtained had a 793 nm LSPR peak (Fig. 12(a)) and 45±7.58 nm length and 9±2.17 nm width on average (Fig. 12(b)).

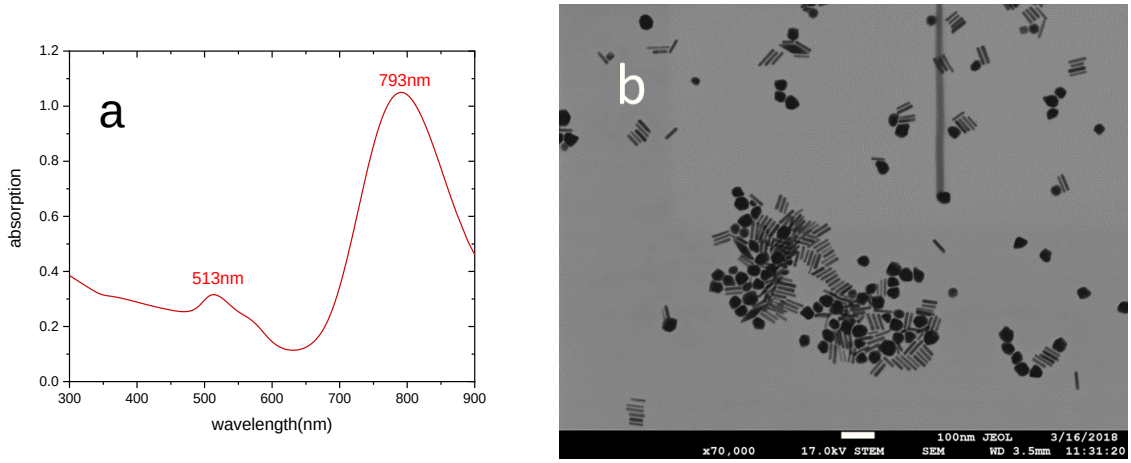

Fig. 12 (a)UV-Vis spectrometry curve of nanorods synthesized with 800nm growth recipe. TSPR peak at 513nm and LSPR peak at 793nm. (b)Scanning Electron Microscope image of the same batch of nanorods containing spherical byproducts

In Fig 12(b) shows the STEM image of as-synthesized AuNRs. The overall rod product yielded at about 75%, the other 25% were spherical byproducts. In this case, the mass of spherical byproducts (diameter about 50 nm) was estimated to be about 17 times heavier than the rod products. So with a certain centrifuge speed and time, the spherical byproducts should settle out before the AuNRs did. The optimized parameter for this separation process was 2000 xg, 8 min at 25 ^{o}C. After centrifuging,

there was a distinct separation between a dark purple colored sediment pellet at the bottom and a brown-colored supernatant as shown in Fig. 13. According to the UV-Vis spectrum, the shoulder peak at 550 nm in as-synthesized AuNRs UV-Vis spectrum was eliminated after the separation. The 550 nm peak in sediment part had a higher intensity which means most of the spherical byproducts were collected in the sediment part. The supernatant that contains over 90% rods and very small amount of byproducts can be collected.

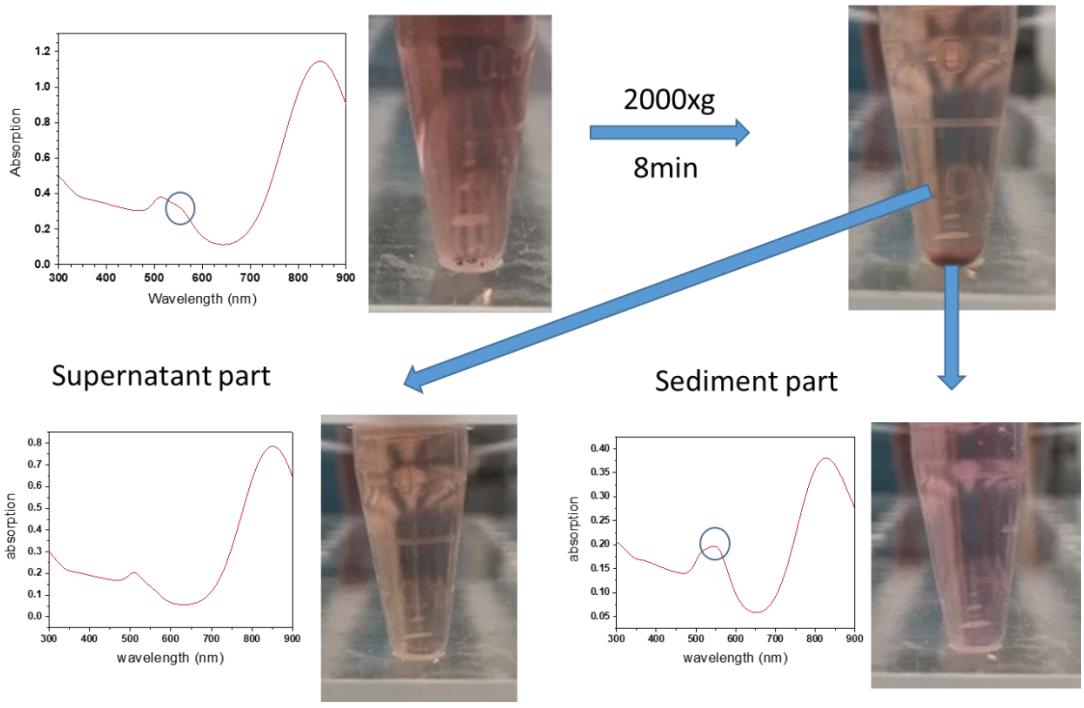

Fig. 13 Schematic of centrifuging-based separation between rods and spherical byproducts. The blue circle on the UV-Vis spectrum indicates absorption peak correspond to spherical gold nanoparticels

Synthesized AuNRs length can be controlled by adjusting the seed amount added into the growth solution. Less seed means less crystallization centers, which gives longer rods with limited amount of Au^{3+} in growth solution. The 880 nm recipe gave us longer AuNRs however yields a bit lower in rod production. This result can be proved from both SEM and UV-Vis results. In the SEM image Fig. 14(b), we could visibly see more spherical and cubic shaped byproducts. In the UV-Vis spectrometer result, the TSPR peak at about 520 nm was clearly broadened comparing to previous one. This was also

evidence for low nanorod yield because TSPR peak of AUNRs has a big overlap with typical absorption peak for spherical byproducts which is about 540nm.

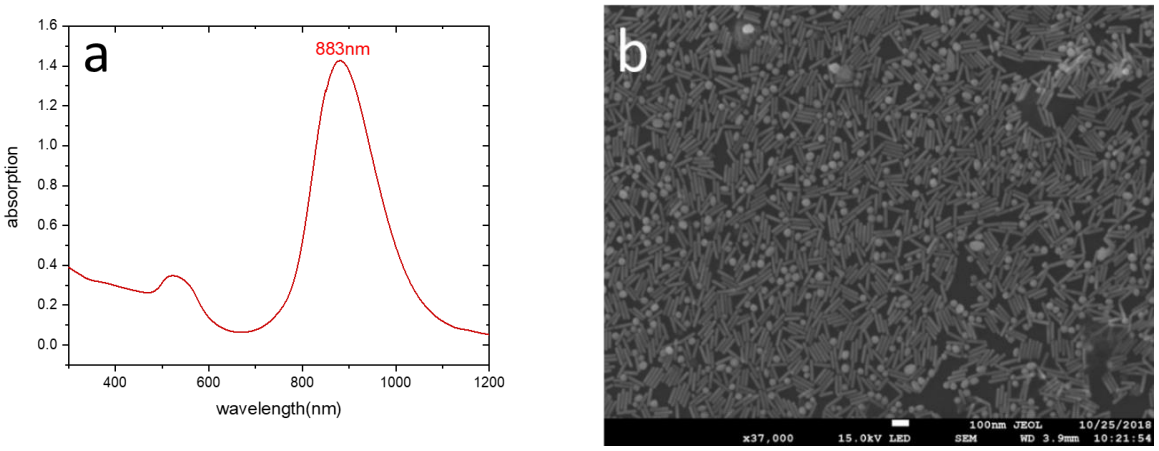

Fig. 14 (a) UV-Vis spectrom (b) SEM image of rods synthesized with 880 nm growth solution recipe.

The 1100 nm AuNRs growth recipe is based on a different reducing agent: hydroquinone rather than $NaBH_4$. Since hydroquinone's reducing strength is limited by the pH environment, we can manipulate the reduction process by adjusting pH in growth solution. As HCl was applied, reducing strength of hydroquinone was lowered in order to get a slower growth, resulting AuNRs with length more than 100 nm on average as shown in Fig. 15.

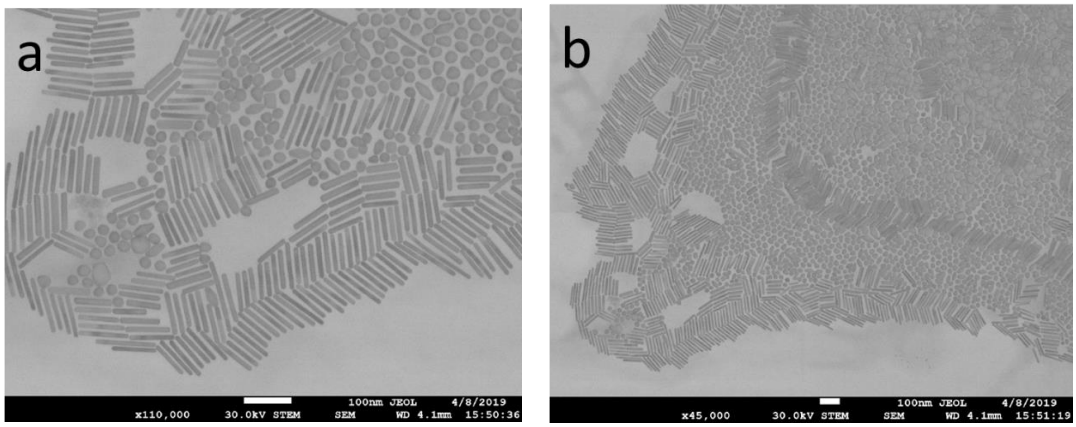

Fig. 15 (a)AuNRs synthesized from 1100nm recipe. (b)Larger scale image

Although AuNRs can be successfully synthesized with extreme length by tuning the pH further, it was found that the yield of rods continued decreasing while increasing the rod length (the rod yield in the 1100 nm rod synthesize sample is lower than 10%) as shown in Fig 15(b).

3.2 Layer-by-layer

Layer-by-layer loading was carried out by coating positive (PDADMAC) and negative (PSS) polyelectrolyte repeatedly. Because the nature of CTAB bilayer as positively charged, the loading process was started from negative PSS layer.

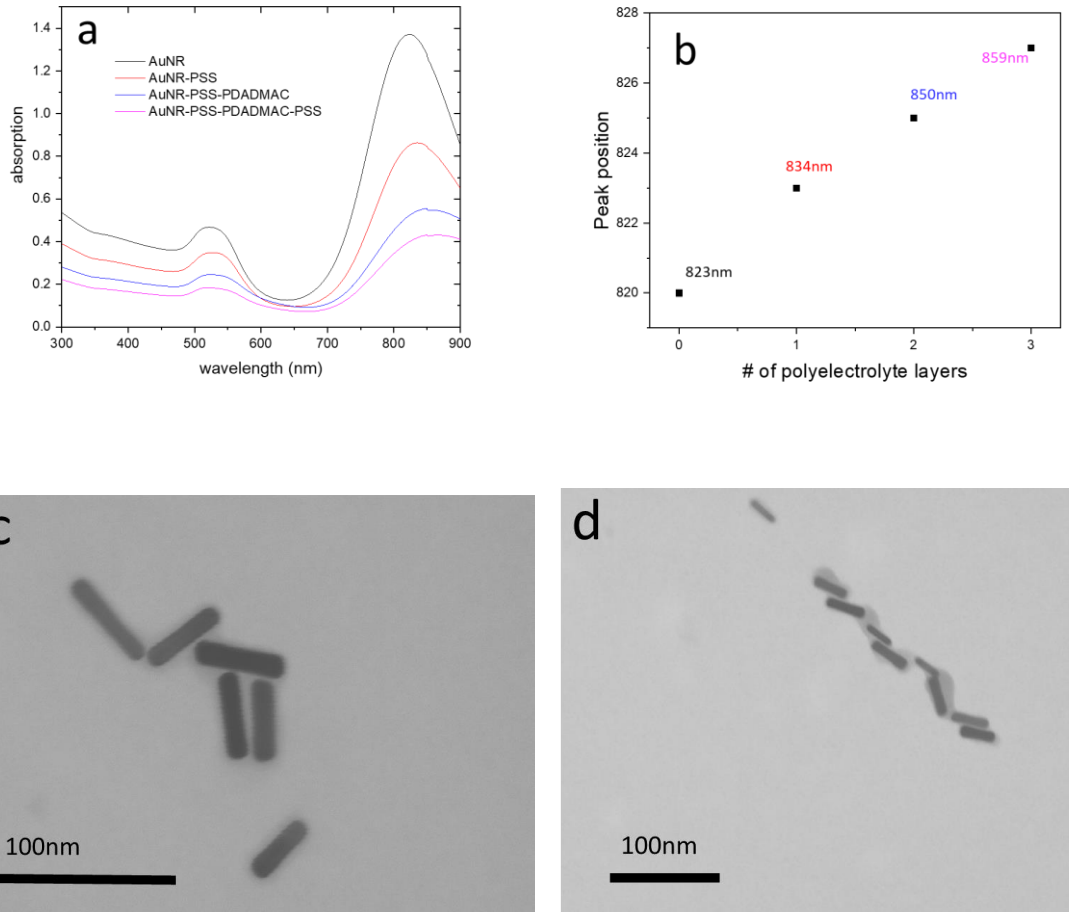

Fig. 16 (a) UV-Vis absorption curve of AuNRs loaded with different number of layers polyelectrolytes (b) The shift of LSPR peak comparing to its origin location (c) STEM image of AuNRs after loading two layers of polyelectrolytes (d) AuNRs with three layers of polyelectrolytes

From the UV-Vis result (Fig. 16(a)) the trend of LSPR peak shifting can be seen as increasing number layers of polyelectrolytes were loaded on the surface of AuNRs. The amount of shifting according to each layer were conducted in Fig. 16(b). Decrease in overall absorption indicates that we were constantly losing AuNRs as we loaded more layers because of the nature of purification process. The peak position change can be explained by the increase of the local dielectric function, it resulted in a red-shift of the nanocrystal plasmon band.[61] The AuNR samples loaded with multiple layers of polyelectrolytes were characterized with STEM. Images were analyzed with ImageJ to conduct the polyelectrolyte layer thickness on the AuNRs surface. An average thickness of 6.10 nm ±1.24 nm was measured for the AuNRs with two layers and 6.91 nm ±1.20 nm for the three layer ones. Also, it is worth mentioning that in the three layer sample, there was an excessive amount of polyelectrolytes which make the shell thickness less uniform.

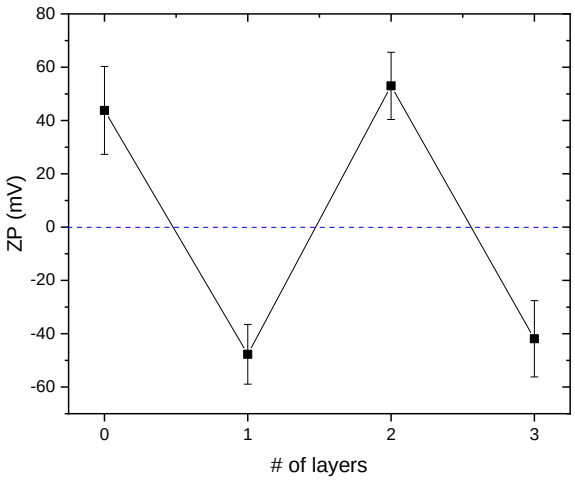

Fig. 17 Zeta-potentiometer result

In order to gain further understanding into the polyelectrolyte layers, the surface charge of modified AUNRs was measured using a Zeta-potentiometer. As shown in Fig. 17 the positive/negative oscillation in potentiometer results further suggested that the layer-by-layer loading process is successful. Also,

because the surface charge for all three modified samples were in a relative narrow range (absolute value about 45 mV), strongly indicating the loading of each layer is quite uniform.

3.3 Mercury sensing

Mercury sensing was carried out by mixing purified AuNR solution with standardized Hg^{2+} water sample. Hg^{2+} ranging from 0.01 M to 2.5 μM (blank was also included as control group) were tested and characterized with UV-Vis spectroscopy. Absorption curve shown in Fig. 18(a) correspond to LSPR peak position shifting from 817 nm in blank 676 nm in 0.005 M Hg^{2+}. The LSPR peak position of 0.01 M Hg^{2+} was not included for the fact that the longitudinal peak completely disappeared on this curve. This is because the Hg^{2+} concentration in this sample was so high that all the AuNRs would be deformed into spherical shaped Hg-Au nanoparticles after being reduced. Also, if we look into the absolute peak intensity ratio LSPR/TSPR also decreased from about 2.81 to 1.00 which resulting from not only LSPR peak lowering but also TSPR increasing. Both of the above results have proven the overall change in average aspect ratio among AuNRs. Notice the increase in TSPR peak, which strongly indicates the width of AuNR increasing as Hg^{2+} concentration getting higher.

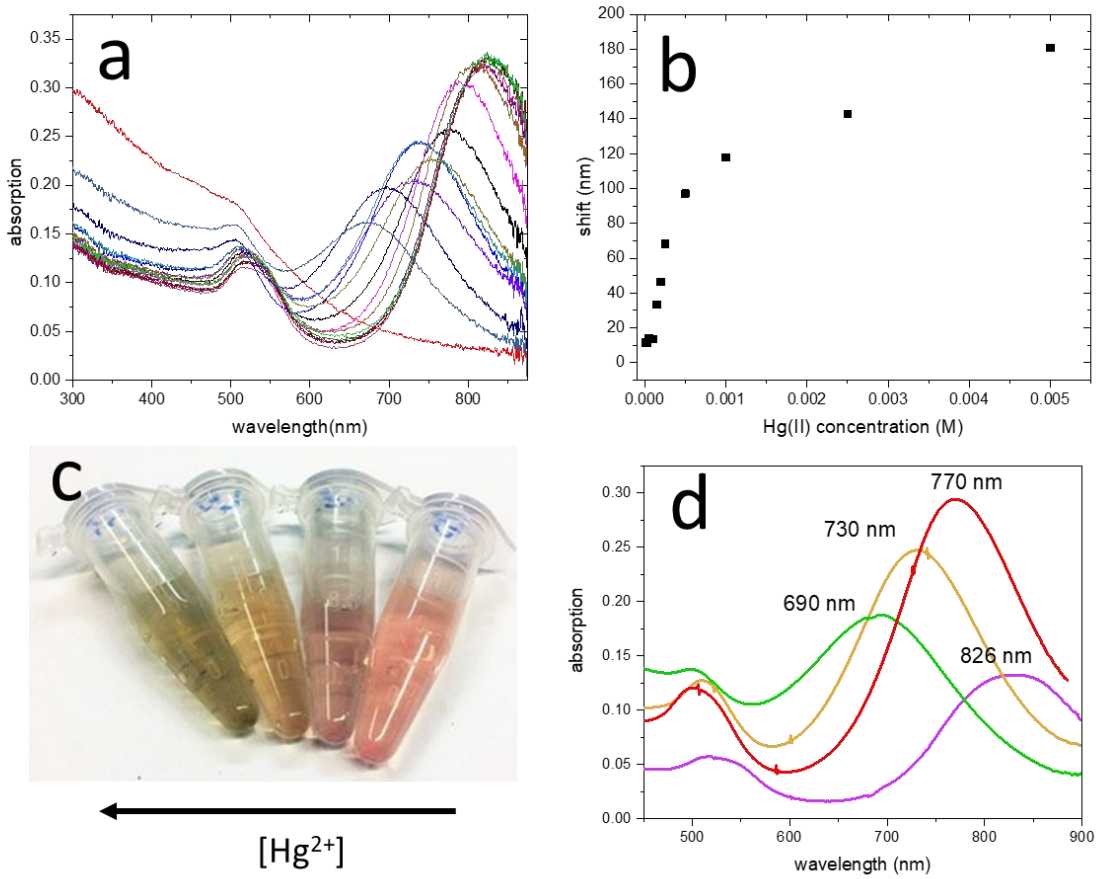

Fig. 18 (a) UV-Vis spectrum of AuNR mixed with Hg^{2+} ranging from 0.01 M to 2.5 μM (b) LSPR peak shift versus the Hg^{2+} concentration (c) AuNR solution color change after being mixed with different amount of Hg(II) (d) UV-Vis spectrum correspond to four samples in previous image

In Fig. 18(b) shows the LSPR peak shift amount versus Hg^{2+} concentration in samples. The peak started to slow down over 0.5 mM and hit saturation above 0.005 M which also suggested AuNRs have reached almost spherical shape at 0.01 M as shown in Fig. 19(b). The LSPR peak shift amount in higher Hg(II) molarity is high enough to being a visible color change to AuNRs solution as shown in Fig. 18(c).

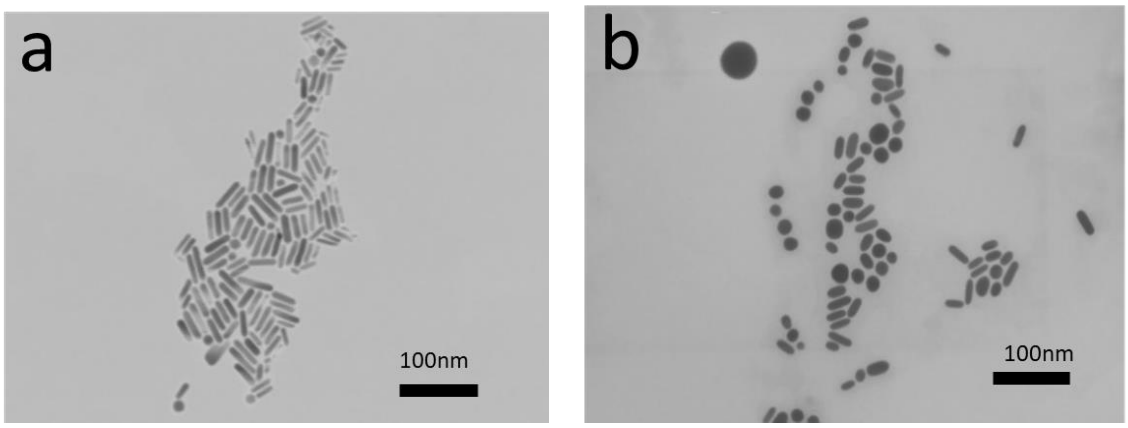

Fig. 19 (a) STEM image of AuNRs used for mercury sensing, (b) AuNRs after mercury sensing, Hg^{2+} concentration at 0.005 M

Further characterization was carried out with STEM. Multiple STEM images were taken for different Hg^{2+} concentrations. Length and width of AuNRs were measured independently, and correspond Hg^{2+} concentration to AR. The relatively large standard deviation in AR came from the non-uniform deformation of all AuNRs. For example in Fig. 19(b), most of the nanoparticles observed are spherical but there are still multiple rod shaped particles.

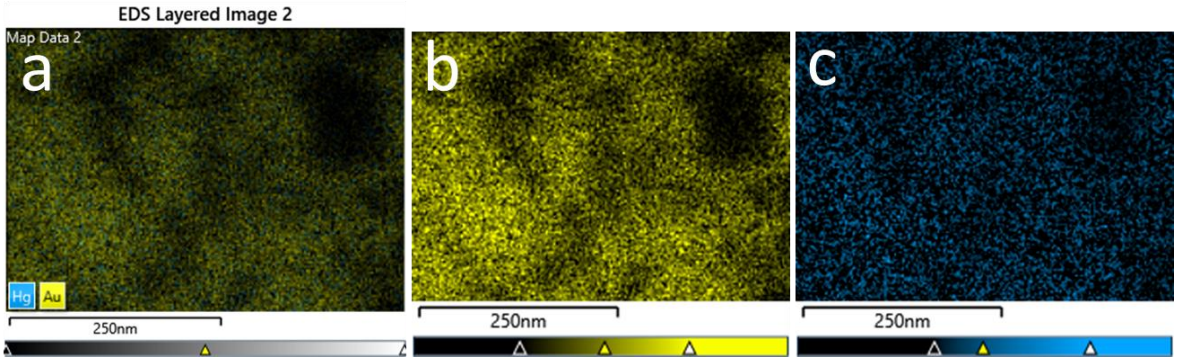

Fig. 20 (a)EDS elemental mapping Hg/Au overlay, (b) Au elemental mapping, (c)Hg elemental mapping

The EDS result shown in Fig. 20 showed a strong indication of Au and Hg element overlapping with each other in a AuNR sample after mercury sensing process. By comparing Fig. 20(b) and (c), most of Hg signal came from where Au was present, which indicates the amalgamation process happened

before imaging. Brighter yellow color in Fig. 20(a) meant intensity of Au signal is stronger than Hg. According to this EDS result, the weight percentage of Au (60 wt%) was about ten times comparing to Hg (6 wt%).

The length and width change through mercury sensing process were traced by measuring STEM image with ImageJ. The result shown in Fig. 21 shows the trend of length, width and aspect ratio change at different Hg^{2+} concentration. As Hg^{2+} concentration increased, the length decreased from 45 nm to 37 nm while the width of the nanorods increased from 8.5 nm to 14 nm. So the aspect ratio change primarily came from the width increase after mercury sensing.

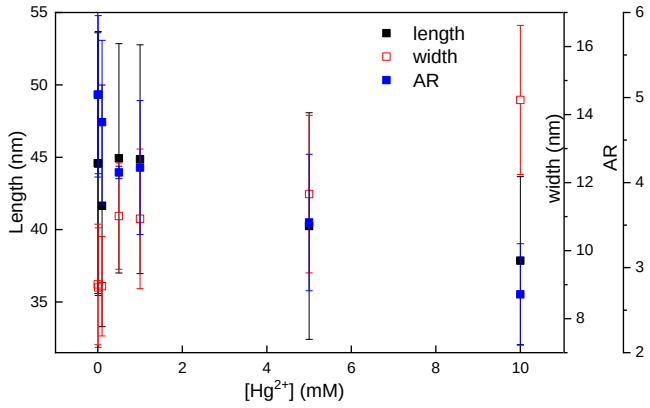

Fig. 21 Diagram of length/width/AR change after mercury sensing at different concentration

While more and more mercury ion sensing results with CTAB-bilayer stabilized AuNRs were accumulated, the reproducibility was consistently poor. At first, the idea was it might be due to the nature of AuNRs synthesized because there were variations in terms of length/width of AuNRs. This variation was eliminated by using AuNRs come from same synthesis batch but it did not contribute to stability. Next step was eliminating the possibility of error during sensing procedure, yet the result still seems to have a wider range than ideal. In the end, the main focus was turned onto the nanoparticle stabilizing agent-CTAB. In synthesis procedure over-concentrated CTAB was used to stabilize reduced nanoparticles and centrifuging process was introduced to get rid of excess CTAB afterwards. Yet, the amount of CTAB taken away using centrifuging purification depends on the

maximum amount of supernatant being taken out when micro pipetting. In other words, the CTAB residue amount in solution could not be quantified. This became problematic because at least a certain amount of CTAB is required in solution to act as a stabilizing agent on AuNR surface. Meanwhile, interaction between CTAB and AuNRs based on Br^- adsorption on gold is not strong enough to sustain multiple centrifuging. According to the experience done, most of the AuNRs solution would start to aggregate starting from the third centrifugation of the particles. In attempt to quantify how much side effect the residue of CTAB has on the mercury sensing process, we re-dispersed the small pellet that contains all AuNRs into different concentrations of CTAB solutions then re-run the whole sensing process. The result clearly indicates CTAB residue amount plays a role in terms of sensing results (Fig. 22). Any concentration over 5 mM will make sensitivity significantly lower. The threshold from this graph is also the minimum amount CTAB needed to stabilize AuNR solution.

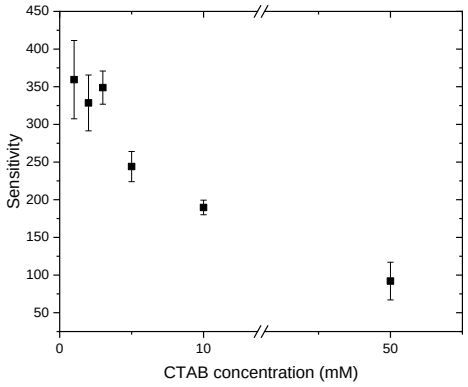

Fig. 22 Mercury sensor sensitivity at different CTAB concentration

Applying polyelectrolytes layers on top of the CTAB-bilayer made the sensing result even more chaotic as more layers of polyelectrolytes were applied as shown in Fig. 23. This instability might also be one of the side effects of our purification process since we did use the same method to purify all the LbL-modified AuNRs.

That being said, centrifuging is still the best/most efficient way to purify. Since the main problem we have on CTAB ligand is its weak interaction on gold surface. We considered it would work better if CTAB is replaced with a ligand that has stronger bond to gold and hence can endure more thorough centrifuging purification.

Since thiol group on the end of a PEG-thiol has strong affinity to gold (the chemisorption between gold and sulfur), the ligand exchange process is simple and time-efficient. PEG-thiol was added into solution to activate a one-step ligand exchange process, then the same purification process was carried out. PEG-thiol stabilized AuNRs can go through centrifuge purification more than 3 times compared to 2 times in most CTAB loaded rods.

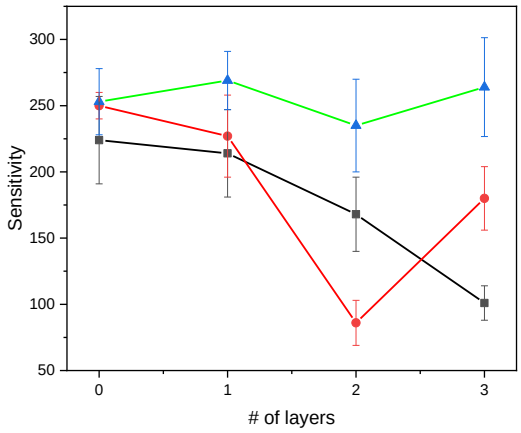

Fig. 23 Sensitivity of AuNRs after deposited with increasing layers of polyelectrolytes

There was a positive side effect of this ligand exchange: not only has the stability issue been solved, the sensitivity of the mercury sensor is increased after ligand exchange.

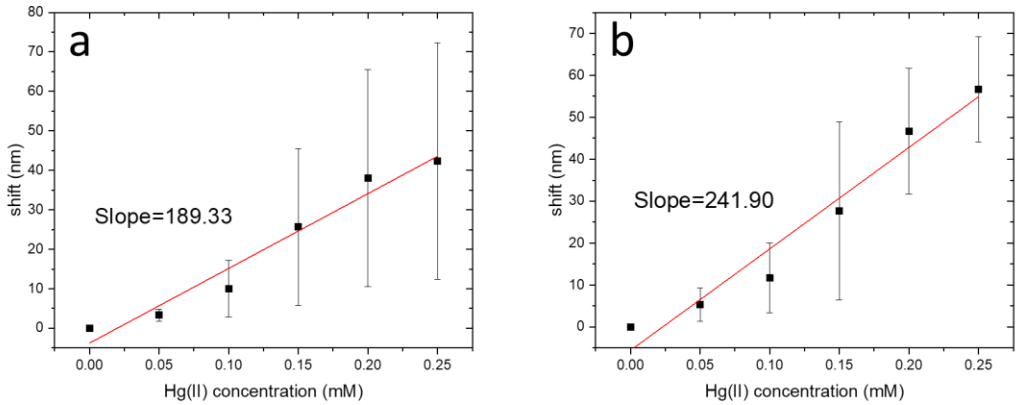

Fig. 24 Mercury sensing result summary of (a) CTAB stabilized AuNR and (b) PEG-Thiol stabilized AuNR

From a comparison between Fig. 24(a) and (b), there were smaller standard deviation on almost all data points. The sensitivity, or the overall slope of the linear fitted line, is substantially higher than before ligand-exchange.

Two possible reasons were proposed about why the sensitivity is increased after ligand-exchange: a) the elimination of the shielding effect from the CTAB bi-layer and, b) the possibility of a greater affinity of thiol groups for Hg^{2+} over the AuNR surface, thus removing PEG-thiol from the surface of the AuNRs made more free space for $Hg^{(0)}$ adsorption. Recently, the formation of mercury sulfide (HgS) directly from linear Hg(II)-thiolate complexes ($Hg(SR)_2$) in natural organic matter and in cysteine solutions was demonstrated under aerated conditions.[62] Repetition of this mechanism leads to the formation of RS-(HgS)n-R chains which may self-assemble in parallel arrays to form cinnabar (α-HgS), or more commonly, quickly condense to four-coordinate metacinnabar (β-HgS).[63] We proposed in our mercury sensing system Hg^{2+} will form RS-Hg^{2+}-RS chains before it was reduced by $NaBH_4$. This might result in the increase in terms of sensitivity and the variant when we incubate Hg^{2+} with AuNR solution for different time length as shown in Fig. 26.

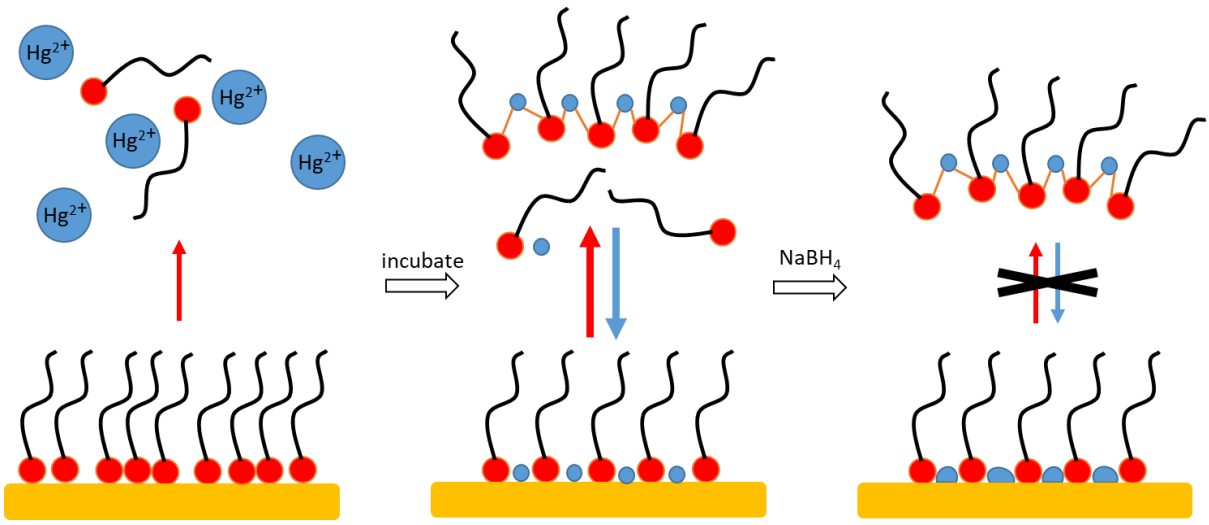

Fig. 25 Schematic of complex forming and equilibrium switching process

In order to test this hypothesis, the experiment for mercury-thiol complexation was designed. After observing the variation in results when we incubate Hg^{2+} with AuNR solution, we tested a series of sensing results. The results corresponding to 0, 20, 40, 60 minutes time interval incubation between PEG-SH-AuNRs and Hg^{2+} solution were shown in Fig. 26.

From the comparison it is obvious that the "linear region" of each curve tend to shift in horizontal direction, which means this "linear region" with steeper slope than other region exists in different Hg^{2+} concentration region. The basic trend in this comparison told us that longer incubation time will bring the "linear region" to lower mercury concentration or, shift to left on X-axis.

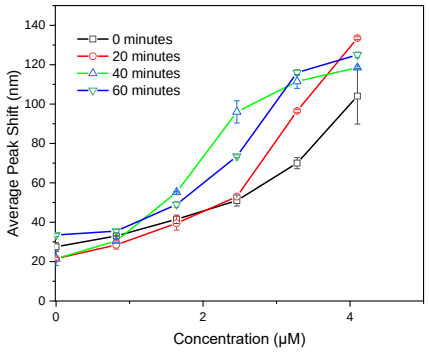

Fig. 26 LSPR peak shift for different incubation time interval

This phenomena can be explained by the nature of complexiation time span. The schematic in Fig. 25 showed this process: the PEG-thiol ligands on AuNRs surface were at equilibrium with the PEG-thiol ligands in solution, then Hg(II) ions were introduced and started to form complex with PEG-thiols in solution which moved the equilibrium towards solution. Under this condition, because the ligands on AuNRs surface were detaching into solution which led to larger effective area for amalgamation, the process became more efficient.

As the incubation time increased, the "linear region" shift to lower concentration could be explained by this model. Longer incubation time meant the equilibrium moved more readily and more exposed surface area on AuNRs where amalgamation happens. But this model cannot explain the shift back at 60 min very well. Presumably when the new equilibrium point is achieved, incubation time shouldn't

cause any impact on the sensing result. This result might indicate the model we used to explain this phenomena is not complete. More experiment will be done to verify this.

3.4 Selectivity

Selectivity test is carried out by mixing AuNR sensor in the exact under same condition with other metallic ions. We chose Ag^{+}, Cr^{3+}, Fe^{3+}, Ba^{2+} and Na^{+} for comparison. The results were characterized in UV-Vis spectrometer and comparing the LSPR peak shift. In theory, because our AuNR sensor is based on amalgam between mercury and gold, which is a very specific process, this system should have outstanding selectivity on mercury ions.

As expected, the AuNR sensor showed strong affinity towards mercury ions. In Fig. 27(b), mercury showed an average of 43 nm of shift at 3 μM of Hg^{2+} concentration while all of other metallic ions made a shift no more than 3 nm at same concentration. The CTAB coated AuNR sensing system also showed a relatively strong selectivity towards Hg^{2+} yet the shift on Hg^{2+} peak is only about 2 times compared to Ag^{+} and Cr^{3+}.

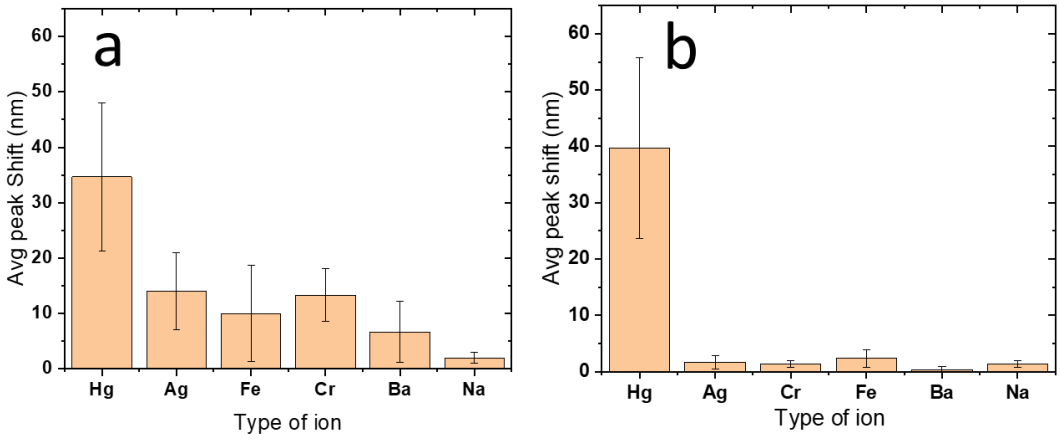

Fig. 27 Selectivity comparing between multiple types of ions (all ion concentration at 3μM) with (a) CTAB coated AuNRs and (b) PEG-Thiol coated AuNRs

Chapter 4. Conclusion and outlook

4.1 Conclusion

In conclusion, we successfully carried out the basic CTAB stabilized AuNR based mercury sensor. The mechanism of mercury amalgamation on AuNR was also studied with the help of EDS detector and mercury etching was proven to be homogeneous on all directions. Two types of AuNRs surface modification methods were done which includes: polyelectrolytes layer-by-layer deposition and PEG-SH ligand exchange. The layer-by-layer process was proven to be successful judged from the UV-Vis spectrum and Zeta-potential results. Yet the attempt of applying layer-by-layer deposited AuNRs into mercury sensing was not ideal. The results were getting more chaotic as more polyelectrolytes layers were deposited.

This phenomena was presumed to be a result of unstable CTAB residue amount after a number of excess purifications done through layer-by-layer loading process. Ligand-exchange process was proposed to address this problem. PEG-thiol was picked as new ligand to swap CTAB bilayer for its strong affinity to gold and water solubility.

Mercury sensing process was also carried out with PEG-thiolated AuNRs and the result showed mercury sensor based on thiolated AuNRs are superior to CTAB-AuNR in mercury sensing. The PEG-thiolated AuNRs possess higher sensitivity, higher stability and better selectivity which needs to be further evaluated by mixing AuNRs with more complicated water sample (or even actual water sample taken from nearby lake/bay area). The reason behind those advantages were also studied. An experiment was designed to study the potential interactions between thiol groups on PEG-thiol ligands and mercury ions. From the preliminary results, the complexation between thiol groups and mercury ions was presumed but still needs further evaluation.

4.2 Outlook

Better understanding in mercury-AuNP interaction process is going to help all the future work related to amalgam process in nanoscale. The final goal of real-time monitoring amalgamation process is still attractive and can be achieved by using advanced instrumentation. The proposed thiol-Hg(II)-thiol complex model can explain most of the results obtained yet still needs to be looked into. More experiments needs to be designed in order to prove the credibility of this model. Surface Enhanced Raman Spectrum (SERS) is now the top candidate for this purpose. Layer-by-layer loaded AuNRs did not behave as expected in mercury sensing yet still have great potential in applications like self-assembly and optical thermal imaging. Both the CTAB stabilized AuNRs and the PEG-thiolated AuNRs based mercury sensor now has a limit of detection at μM range which is not comparable with cold-vapor AAS's pM for now. But this system provides a good platform for water quality test that doesn't require expensive instrument and can also make a perfect analytical chemistry experiment for education purposes.

Works Cited

1. Faraday, M. The Bakerian Lecture. —Experimental Relations of Gold (and Other Metals) to Light. *Philosophical Transactions of the Royal Society of London* **1857**, *147*, 145–181.
2. C. S. Thaxton, et al., Nanoparticle-based bio-barcode assay redefines "undetectable" PSA and biochemical recurrence after radical prostatectomy. *PNAS* November 3, **2009** 106 (44) 18437-18442
3. *NSF* Workshop on Catalysis. http://www.che.caltech.edu/nsfcatworkshop/#Reports (accessed July 18th. 2019)
4. Gogotsi, Y. *Nanomaterials handbook*; CRC Press: Boca Raton, 2006.
5. Cao, G. *Nanostructures and Nanomaterials*; Imperial College Press: London, 2004.
6. Sakka, S. *Handbook of sol-gel science and technology: processing, characterization and applications*; Kluwer: Boston, 2005.
7. Turkevich, J.; Stevenson, P. C.; Hillier, J. A Study of the Nucleation and Growth Processes in the Synthesis of Colloidal Gold. *Discussions of the Faraday Society* **1951**, *11*, 55.
8. *Reviews of modern physics*; Published for the American Physical Society by the American Institute of Physics: Lancaster, P.A., 1969.
9. Li, Y.; Somorjai, G. A. Nanoscale Advances in Catalysis and Energy Applications. *Nano Letters* **2010**, *10*(7), 2289–2295.
10. Laird, E. A., Kuemmeth, F., Steele, G. A., Grove-Rasmussen, K., Nygård, J., Flensberg, K., & Kouwenhoven, L. P. Quantum transport in carbon nanotubes. *Reviews of Modern Physics* **2015**, 87(3), 703-764
11. Rao, C. N. R.; Govindaraj, A. *Nanotubes and nanowires*; RSC: Cambridge, 2005.
12. Baughman, R. H. Carbon Nanotubes--the Route Toward Applications. *Science* **2002**, *297*(5582), 787–792.
13. Kasumov, A. Superconductivity in Ropes of Single-Walled Carbon Nanotubes. *Physica B: Condensed Matter* **2003**, *329-333*, 1321–1322.
14. Kliewer, C. J.; Somorjai, G. A. Structure Effects on Pyridine Hydrogenation over Pt(111) and Pt(100) Studied with Sum Frequency Generation Vibrational Spectroscopy. *Catalysis Letters* **2010**, *137*(3-4), 118–122.
15. Link, S.; El-Sayed, M. A. Optical Properties and Ultrafast Dynamics of Metallic Nanocrystals. *Annual Review of Physical Chemistry* **2003**, 54:331-366.
16. Jain, S.; Hirst, D. G.; O'Sullivan, J. M. Gold nanoparticles as novel agents for cancer therapy. *The British Journal of Radiology*2012, 85(1010), 101-113
17. Shen, Y. R. Surface Properties Probed by Second-Harmonic and Sum-Frequency generation. *Nature* **1989**, *337*(6207), 519–525.
18. Aslan, K.; Lakowicz, J. R.; Geddes, C. D. Plasmon Light Scattering in Biology and Medicine: New Sensing Approaches, Visions and Perspectives. *Current Opinion in Chemical Biology* **2005**, *9*(5), 538–544.
19. Prucker, O.; Naumann, C. A.; Rühe, J.; Knoll, W.; Frank, C. W. Photochemical Attachment of Polymer Films to Solid Surfaces via Monolayers of Benzophenone Derivatives. *Journal of the American Chemical Society* **1999**, *121*(38), 8766–8770.
20. Kleinman, S. L.; Sharma, B.; Blaber, M. G.; Henry, A.-I.; Valley, N.; Freeman, R. G.; Natan, M. J.; Schatz, G. C.; Duyne, R. P. V. Structure Enhancement Factor Relationships in Single Gold

Nanoantennas by Surface-Enhanced Raman Excitation Spectroscopy. *Journal of the American Chemical Society* **2012**, *135*(1), 301–308.
21. Mahmoud, M. A.; Oneil, D.; El-Sayed, M. A. ChemInform Abstract: Hollow and Solid Metallic Nanoparticles in Sensing and in Nanocatalysis. *ChemInform* **2014**, *45*(9).
22. Ma, X.; He, S.; Qiu, B.; Luo, F.; Guo, L.; Lin, Z. Noble Metal Nanoparticle-Based Multicolor Immunoassays: An Approach toward Visual Quantification of the Analytes with the Naked Eye. *ACS Sensors* **2019**, *4*(4), 782–791.
23. Freestone, I.; Meeks, N.; Sax, M.; Higgitt, C. The Lycurgus Cup — A Roman Nanotechnology. *Gold Bulletin* **2007**, *40*(4), 270–277.
24. Löwenstern-Kunckel, J. Öffentliche Zuschrift von dem Phosphor Mirabil. **1678**
25. Turkevich, J.; Stevenson, P. C.; Hillier, J. A Study of the Nucleation and Growth Processes in the Synthesis of Colloidal Gold. *Discussions of the Faraday Society* **1951**, *11*, 55.
26. Foss, C. A.; Hornyak, G. L.; Stockert, J. A.; Martin, C. R. Template-Synthesized Nanoscopic Gold Particles: Optical Spectra and the Effects of Particle Size and Shape. *The Journal of Physical Chemistry* **1994**, *98*(11), 2963–2971.
27. Xia, Y.; Halas, N. J. Shape-Controlled Synthesis and Surface Plasmonic Properties of Metallic Nanostructures. *MRS Bulletin* **2005**, *30*(5), 338–348.
28. Jana, N. R.; Gearheart, L.; Murphy, C. J. Seed‐Mediated Growth Approach for Shape‐Controlled Synthesis of Spheroidal and Rod‐like Gold Nanoparticles Using a Surfactant Template. *Advanced Materials* **2001**, 13(18), 1389-1393
29. Aberasturi, D. J. D.; Serrano-Montes, A. B.; Liz-Marzán, L. M. Modern Applications of Plasmonic Nanoparticles: From Energy to Health. *Advanced Optical Materials* **2015**, *3*(5), 602–617.
30. Lal, S.; Grady, N. K.; Kundu, J.; Levin, C. S.; Lassiter, J. B.; Halas, N. J. ChemInform Abstract: Tailoring Plasmonic Substrates for Surface Enhanced Spectroscopies. *ChemInform* **2008**, *39*(32).
31. Hamon, C.; Novikov, S.; Scarabelli, L.; Basabe-Desmonts, L.; Liz-Marzán, L. M. Hierarchical Self-Assembly of Gold Nanoparticles into Patterned Plasmonic Nanostructures. *ACS Nano* **2014**, *8*(10), 10694–10703.
32. Wickham, J.; Alivisatos, A. P. Kinetics of II-VI and III-V Colloidal Semiconductor Nanocrystal Growth: "Focusing" of Size Distributions. *J. Am. Chem. Soc.* **1998,** 120(21), 5343-5344
33. Johnson, C. J.; Dujardin, E.; Davis, S. A.; Murphy, C. J.; Mann, S. Growth and Form of Gold Nanorods Prepared by Seed-Mediated, Surfactant-Directed Synthesis. *Journal of Materials Chemistry* **2002**, *12*(6), 1765–1770.
34. Xiong, Y.; Cai, H.; Wiley, B. J.; Wang, J.; Kim, M. J.; Xia, Y. Synthesis and Mechanistic Study of Palladium Nanobars and Nanorods. *Journal of the American Chemical Society* **2007**, *129*(12), 3665–3675.
35. Bullen, C.; Zijlstra, P.; Bakker, E.; Gu, M.; Raston, C. Chemical Kinetics of Gold Nanorod Growth in Aqueous CTAB Solutions. *Crystal Growth & Design* **2011**, *11*(8), 3375–3380.
36. Mie, G. Beiträge Zur Optik Trüber Medien, Speziell Kolloidaler Metallösungen. *Annalen der Physik* **1908**, *330*(3), 377–445.
37. Goldman, L.; Rockwell, R.J. Jr. Laser systems and their applications in medicine and biology. *Adv Biomed Eng Med Phys* **1968**, 1, 317-82.
38. Kreibig, U.; Vollmer, M. Optical Properties of Metal Clusters. *Adv. Mater.* **1995**, 203–274.

39. Minamata Disease The History and Measures - Chapter 2. http://www.env.go.jp/en/chemi/hs/minamata2002/ch2.html (accessed Jun 23, 2019).
40. Maprani, A. C.; Al, T. A.; Macquarrie, K. T.; Dalziel, J. A.; Shaw, S. A.; Yeats, P. A. Determination of Mercury Evasion in a Contaminated Headwater Stream. *Environmental Science & Technology* **2005**, *39*(6), 1679–1687.
41. James, J. Z.; Lucas, D.; Koshland, C. P. Gold Nanoparticle Films As Sensitive and Reusable Elemental Mercury Sensors. *Environmental Science & Technology* **2012**, *46*(17), 9557–9562.
42. Cárdenas-Lizana, F.; Gómez-Quero, S.; Perret, N.; Keane, M. A. Support Effects in the Selective Gas Phase Hydrogenation Ofp-Chloronitrobenzene over Gold. *Gold Bulletin* **2009**, *42*(2), 124–132.
43. EPA Method 245.1: Determination of Mercury in Water by Cold Vapor Atomic Absorption Spectrometry. https://www.epa.gov/homeland-security-research/epa-method-2451-determination-mercury-water-cold-vapor-atomic-absorption (accessed Jun 23, 2019).
44. Marine water & sediment monitoring. https://ecology.wa.gov/Research-Data/Monitoring-assessment/Puget-Sound-and-marine-monitoring (accessed Jun 23, 2019).
45. https://apps.ecology.wa.gov/eim/search/Detail/Detail.aspx?DetailType=Result&SystemResultId=93871341 (accessed Jun 23, 2019).
46. https://apps.leg.wa.gov/WAC/default.aspx?cite=173-200-040 (accessed Jun 23, 2019).
47. Patton, G. W.; Crecelius, E. A. Simultaneously Extracted Metals/Acid-Volatile Sulfide and Total Metals in Surface Sediment from the Hanford Reach of the Columbia RIver and the Lower Snake River. **2001**.
48. Atomic absorption spectroscopy. https://en.wikipedia.org/wiki/Atomic_absorption_spectroscopy#Cold-vapor_atomization (accessed Jun 23, 2019).
49. Guidance on Evaluating Sediment Contaminant Results". Ohio Environmental Protection Agency: Division of Surface Water. January 2010
50. http://mine-engineer.com/mining/minproc/MercAmal.htm (accessed Jun 23, 2019).
51. Su, D.; Katsikas, L.; Giersig, M. Formation of Amalgam Particles in Bimetallic Silver and Mercury Colloids. *Berichte der Bunsengesellschaft für physikalische Chemie* **1997**, *101*(11), 1644–1646.
52. Liu, Y.; Huang, C. Z. Real-Time Dark-Field Scattering Microscopic Monitoring of the in Situ Growth of Single Ag@Hg Nanoalloys. *ACS Nano* **2013**, *7*(12), 11026–11034.
53. Wang, J.-G.; Fossey, J. S.; Li, M.; Xie, T.; Long, Y.-T. Real-Time Plasmonic Monitoring of Single Gold Amalgam Nanoalloy Electrochemical Formation and Stripping. *ACS Applied Materials & Interfaces* **2016**, *8*(12), 8305–8314.
54. Slaughter, L. S.; Chang, W.-S.; Swanglap, P.; Tcherniak, A.; Khanal, B. P.; Zubarev, E. R.; Link, S. Single-Particle Spectroscopy of Gold Nanorods beyond the Quasi-Static Limit: Varying the Width at Constant Aspect Ratio. *The Journal of Physical Chemistry C* **2010**, *114*(11), 4934–4938.
55. Solis, D.; Chang, W.-S.; Khanal, B. P.; Bao, K.; Nordlander, P.; Zubarev, E. R.; Link, S. Bleach-Imaged Plasmon Propagation (BlIPP) in Single Gold Nanowires. *Nano Letters* **2010**, *10*(9), 3482–3485.
56. Mayer, K. M.; Hafner, J. H. Localized Surface Plasmon Resonance Sensors. *Chemical Reviews* **2011**, *111*(6), 3828–3857.

57. Rex, M.; Hernandez, F. E.; Campiglia, A. D. Pushing the Limits of Mercury Sensors with Gold Nanorods. *Analytical Chemistry* **2006**, *78*(2), 445–451.
58. Morris, T.; Copeland, H.; Mclinden, E.; Wilson, S.; Szulczewski, G. The Effects of Mercury Adsorption on the Optical Response of Size-Selected Gold and Silver Nanoparticles. *Langmuir* **2002**, *18*(20), 7261–7264.
59. Chang, J.-Y.; Wu, H.; Chen, H.; Ling, Y.-C.; Tan, W. Oriented Assembly of Au Nanorods Using Biorecognition System. *Chemical Communications* **2005**, No. 8, 1092.
60. Häkkinen, H. The Gold–Sulfur Interface at the Nanoscale. *Nature Chemistry* **2012**, *4*(6), 443–455.
61. Nikoobakht, B.; El-Sayed, M. A. Preparation and Growth Mechanism of Gold Nanorods (NRs) Using Seed-Mediated Growth Method. *Chemistry of Materials* **2003**, 15 (10), 1957–1962.
62. Mulvaney, P. Surface Plasmon Spectroscopy of Nanosized Metal Particles. *Langmuir* **1996**, *12*(3), 788–800.
63. Manceau, A.; Lemouchi, C.; Enescu, M.; Gaillot, A.-C.; Lanson, M.; Magnin, V.; Glatzel, P.; Poulin, B. A.; Ryan, J. N.; Aiken, G. R.; Gautier-Luneau, I.; Nagy, K. L. Formation of Mercury Sulfide from Hg(II)–Thiolate Complexes in Natural Organic Matter. *Environmental Science & Technology* **2015**, *49*(16), 9787–9796.
64. Enescu, M.; Nagy, K. L.; Manceau, A. Nucleation of Mercury Sulfide by dealkylation. *Scientific Reports* **2016**, *6*(1).
65. Ye, X.; Zheng, C.; Chen, J.; Gao, Y.; Murray, C. B. Using Binary Surfactant Mixtures To Simultaneously Improve the Dimensional Tunability and Monodispersity in the Seeded Growth of Gold Nanorods. *Nano Letters* **2013**, *13*(2) 765–771.